Beam trapping in a modified betatron accelerator

C. A. Kapetanakos, D. Dialetis,* S. J. Marsh,† L. K. Len,‡ and T. Smith‡
Plasma Physics Division, Naval Research Laboratory, Washington, D.C. 20375-5000
(Received 24 May 1991)

The experimental results on the trapping of the beam in the Naval Research Laboratory modified betatron accelerator are in good agreement with a revised model of resistive trapping, and thus it may be concluded that the wall resistivity is responsible for the inward spiral motion of the beam after injection.

INTRODUCTION

Currently, several laboratories [1–5] are engaged in studies to assess the feasibility of compact, high-current accelerators. Among the various accelerating schemes presently under investigation is the modified betatron accelerator (MBA) [6–8]. This device is under study at the University of California, Irvine [2] and also at the Naval Research Laboratory (NRL). Since the initial successful demonstration of acceleration [1] approximately two years ago, the NRL-MBA has achieved [11] trapped currents as high as 1.5 kA and energies approximately 18 MeV. The beam lifetime that is typically 700–900 μsec is limited by the cyclotron resonance.

Following the installation of strong focusing windings [9,10] in the NRL device it is routinely observed [1,11] that for several combinations of injection parameters the beam consistently spirals from the injection position to the magnetic minor axis and is trapped. The explanation of this interesting phenomenon has been so far elusive. However, a fair understanding of the trapping mechanism is not only of academic interest but a necessity for any upgrading of the existing or the construction of a new device.

In this paper we report recent experimental results on the trapping of the beam in the NRL-MBA. The results are in agreement with a revised model of resistive trapping [12]. Two modifications have been introduced to the original model. First, the beam motion is not limited near the minor axis and therefore nonlinear effects and the fast diffusion times that scale as $\mu_0(b-a)^2/\pi^2\rho$, where $b-a$ is the thickness of the chamber and ρ is the wall resistivity, become important. Second, in order to take into account the intermediate motion [10] of the beam that has been omitted in the calculation of the image fields of the beam, the wall surface resistivity is computed using the skin depth that corresponds to the frequency of the intermediate mode and not the actual thickness of the chamber.

There are three distinct groups of diffusion times with which the self-magnetic-field of the beam leaks out of a resistive torus. The shortest are the "plane" characteristic times

$$\tau_{mk}\approx\mu_0(b-a)^2/\pi^2\rho k^2=\frac{\tau_{01}}{k^2}\equiv\frac{\tau_p}{k^2}\ ,$$

where $k=1,2,3,\ldots$. The "plane" diffusion times are important when the beam is near the wall. The "cylinder" diffusion times are

$$\tau_{m0}\approx\tau_{10}/m=\tau_c/m=\mu_0 a(b-a)/2\rho m\ ,$$

where $m=1,2,3,\ldots$. Both τ_p and τ_c determine the speed with which the self-magnetic-field of the beam penetrates the wall of the chamber and are instrumental in the resistive trapping of the beam. Finally, the "loop" diffusion time $\tau_{00}\equiv\tau_l=2\tau_c(\ln(8r_0/a)-2]$, where r_0 is the major radius of the torus, determines the speed with which the beam field diffuses into the hole of the doughnut. The "loop" diffusion time does not play any role in the resistive trapping of the beam.

The resistive trapping is due to the negative radial component of the image magnetic field of the beam that acts on its centroid, when such a beam moves poloidally inside a resistive chamber. This field component crossed with the axial (toroidal) velocity of the beam produces a poloidal force, which is in the opposite direction to the poloidal motion of the beam. In the absence of the strong focusing and when the self-fields dominate the external fields (high-current regime), the poloidal force in conjunction with the axial (toroidal) magnetic field drives the beam to the wall (drag instability [13]). However, in the presence of strong focusing the direction of the poloidal motion can be reversed and the beam spirals to the minor axis [12].

BRIEF DESCRIPTION OF THE EXPERIMENT

The NRL modified betatron has been described [1,14] previously. In this paper we give, for completeness, a short description of its basic components. The NRL-MBA is a toroidal device that comprises three different external magnetic fields; the betatron field B_z that can vary from 0–2.7 kG, the toroidal field B_θ that can vary between 0–5.1 kG, and the strong focusing field that has a maximum gradient between 0–31 G/cm, when the current I_{SF} in the windings varies from 0–30 kA.

The 100-cm major radius, 15.2-cm-inside minor radius vacuum chamber has been constructed using epoxy-reinforced carbon fibers. The desired conductivity is obtained by embedding in the outer layer of graphite a phosphor bronze screen. The measured dc resistance of the toroidal vessel is 68±2 mΩ and the corresponding

surface resistivity is 10.3 mΩ on a square. The graphite surface resistivity is 26.6 mΩ on a square.

The electrons are emitted from one end-face of a cylindrical carbon cathode. The other end-face is mounded on the cathode stalk. The emitting surface of the cathode faces the circular opening of the conical anode, which is located on the midplane of the device, 8.7 cm from its minor axis.

EXPERIMENTAL RESULTS

Over a wide range of parameters and after fine tuning the external fields the beam spirals from the injector near the minor axis and is trapped. The beam trapping time, i.e., the time it takes the beam to travel from the injection position to the vicinity of the minor axis is determined by measuring the time delay between the x-ray peaks that are generated at injection and at a 1×1.1-cm, 0.8-mm-thick lead target that is located on the magnetic minor axis. The lead target is mounted on the front surface of a 3-μm-thick polycarbonate foil that is stretched across the minor cross section of the vacuum chamber as shown in Fig. 1(a). The x rays are monitored by a collimated x-ray detector that is located 4 m away from the lead target. The scintillator-photomultiplier tube is housed inside a lead box and the x rays enter the scintillator through a 3-mm-diam hole. The foil is graphite coated on the upstream side to avoid charging. Figure 1(b) shows an open-shutter photograph of the light emitted as the beam passes through the foil. The x rays emitted as the beam strikes the diode and the lead target are shown in the upper trace of Fig. 1(c). The trapping time τ_{tr} for this shot is 1.25 μsec. The lower trace of Fig. 1(c) shows the output of the Rogowski coil that monitors the beam current. The peak of the signal corresponds to 1.2 kA.

The results shown in Fig. 1 were taken with a 0.5-cm hole in the anode. This hole is by a factor of 3 smaller than that used regularly in the NRL device. Thus, the trapped current has been reduced by a factor of 2–3. This reduction in the beam current was necessary in order to achieve satisfactory resolution in the open-shutter photographs.

To determine the effect of the foil on the transverse beam orbit, we carried out a series of experiments in which the 3-μm-thick foil was replaced with a foil of the same composition but with only half its thickness. The results show that the equilibrium position of the beam is slightly larger in the case of 1.5-μm-thick foil. It requires approximately 1–2 G higher vertical field (~4–8%) to shift the equilibrium to its original position and make the orbits identical.

As the electrons pass through the plastic foil, they suffer both inelastic and elastic scattering. The stopping power [15] of 0.6 MeV electrons passing through polyethylene (data for polycarbonate are not available) is ~2 (MeV cm^2)/gm. Thus, the energy loss per pass is 0.6 keV. The total energy loss in 1.2 μsec, i.e., in sixty revolutions around the major axis, is 36 keV or ~6%. The energy loss in the thinner foil is only 18 keV and therefore the equilibrium position is expected to increase by

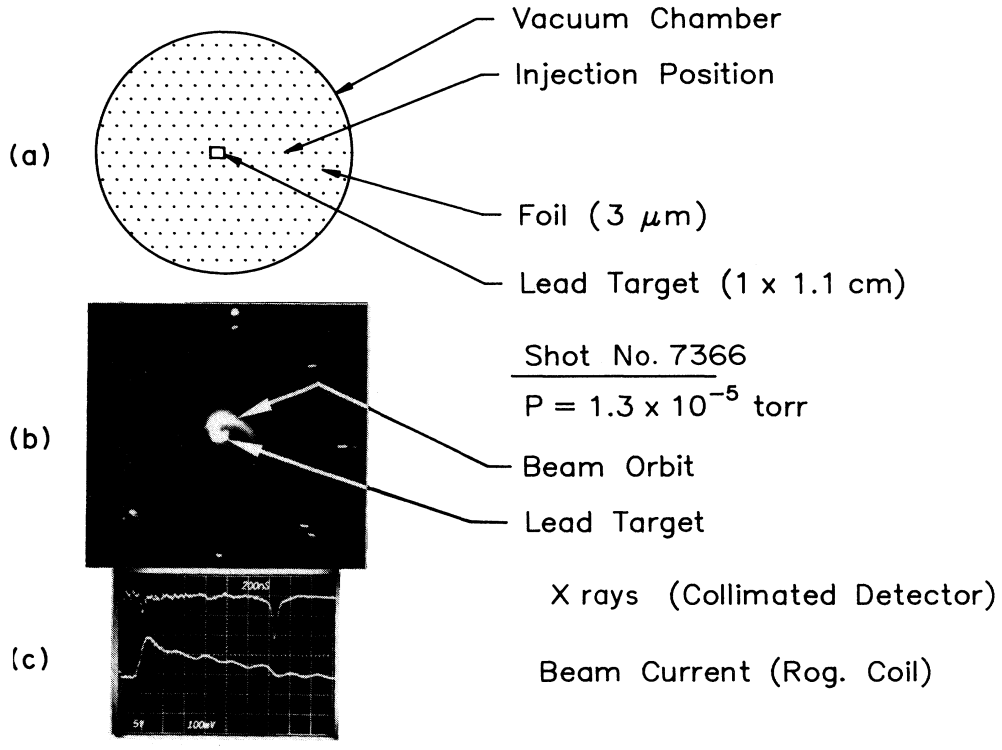

FIG. 1. Beam trapping time.

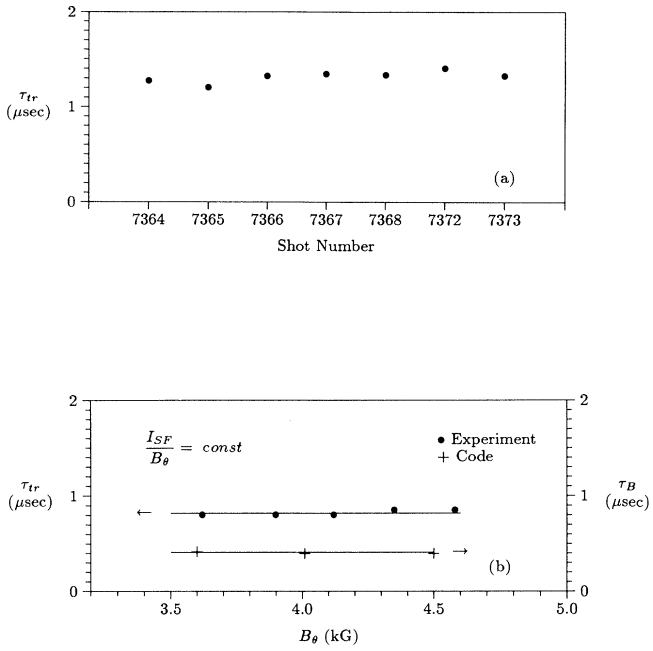

FIG. 2. (a) Trapping time reproducibility and (b) dependence of τ_{tr} and τ_B on B_θ for constant I_{SF}/B_θ.

3% when the thickness of the foil is reduced to half. This shift is not substantially different from that observed in the experiment. The elastic-scattering induced RMS angle is 0.9° for the first pass through the 1.5-μm-thick foil. Although substantial, the elastic scattering does not contribute to the shift of the equilibrium position.

The beam orbits are very reproducible and τ_{tr} shows only modest variations for the same operating parameters. Figure 2(a) shows τ_{tr} for seven shots taken with the same values of the fields. It is apparent from this figure that τ_{tr} varies by $\pm 7\%$. In a second run with five shots the variation was even smaller. Figure 2(b) shows τ_{tr}, vs B_θ for constant I_{SF}/B_θ, where I_{SF} is the current of the strong-focusing windings. For all practical purposes τ_{tr} remains constant in the narrow range tested.

In addition to τ_{tr}, the bounce period τ_B, i.e., the time the beam takes to perform a complete revolution in the poloidal direction, is of special interest. To determine τ_B, the foil target was removed and replaced with a 1.1-cm-wide, 1-mm-thick, 16-cm-long lead strip. The lead target is backed on the upstream side by a thin plastic strip and is mounted on a half lucite ring that is carbon coated. The symmetry axis of the target lies on the midplane of the device as shown in Fig. 3(a).

The light emitted from the upstream side of the target when the beam strikes it is monitored with an open

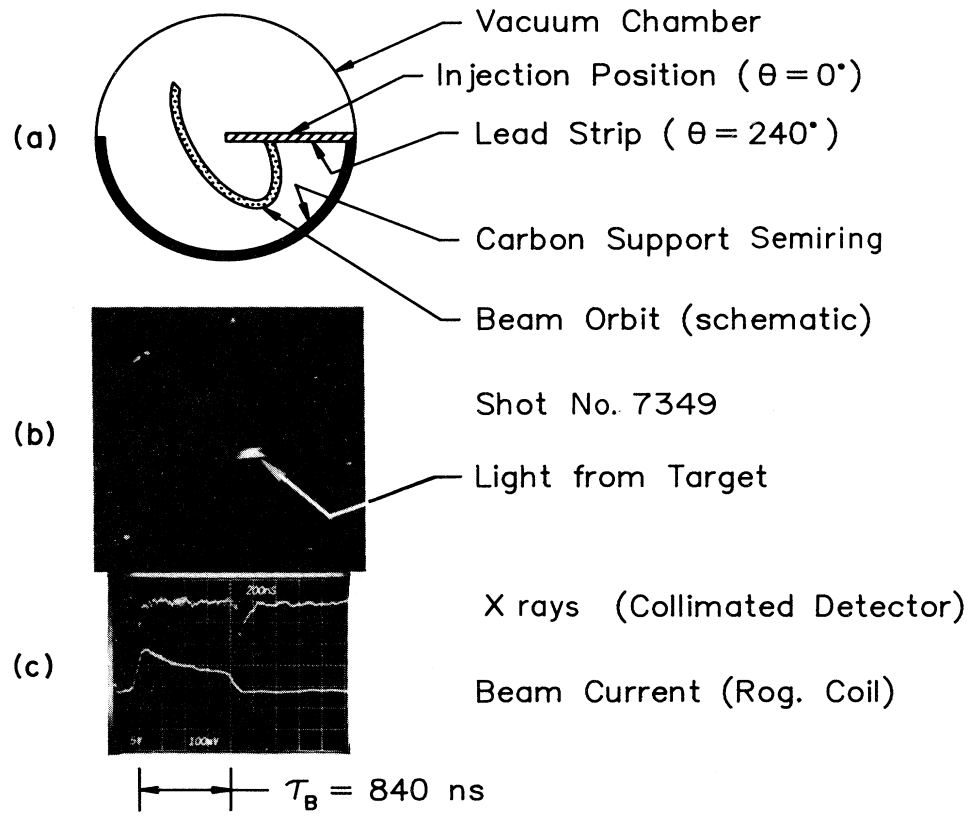

FIG. 3. Beam bounce period.

shutter camera. Results are shown in Fig. 3(b). The x-ray signal and the output of the Rogowski coil that monitors the beam current are shown in Fig. 3(c). The bounce period is inferred from the time delay of the two x-ray peaks, as indicated in Fig. 3(c), and in this shot is 840 nsec. The damage pattern on the lead strip has a diameter that is equal to the diameter of the anode hole. This implies that the diameter of the beam has not changed after about 40 revolutions around the major axis. In addition, we observe that the damage pattern is a semicircle that is always located near the lower edge of the strip. From this observation it may be concluded that the beam drifts 3 mm over 20 nsec, i.e., its bounce speed near the strip is ~ 15 cm/μsec.

To verify that there is no correlation between τ_{tr} and τ_l, i.e., with the speed the beam magnetic field diffuses into the hole of the doughnut, the vacuum chamber was unbolted in two joints that are located 180° apart in the toroidal direction and a ring insulator was inserted in each of these joints. Sixty carbon resistors, 51 Ω each, were symmetrically mounted on the outer surface of one of the two rings as shown in Fig. 4(a). To improve its voltage holding capabilities the inner surface of the blue nylon insulator was angled and a 0.6-cm-deep groove was machined at its plane of symmetry. In addition, its inner surface was protected from stray electrons by a 0.8-mm-thick lead strap that is supported by an epoxy reinforced carbon fiber belt. The purpose of the second insulator was only to minimize the distortion of the toroidal chamber and thus shorting wide straps, instead of resistors, were installed on its outer surface.

There are two distinct currents flowing on the wall of the vacuum chamber. The first i_w is due to the rising vertical field and the second I_r is induced by the beam. Since the vertical field during the first quarter period varies as $B_z(t)=B_{zp}\sin(2\pi t/\tau)$, where B_{zp} is the peak field and τ is the period, the induced voltage in the chamber is $V=-V_0\cos(2\pi t/\tau)$, where $V_0=(4\pi^2 r_0^2/\tau)B_{zp}$, and r_0 is the major radius of the torus. The current flowing on the wall of the chamber is described by the equation $V=L(di_w/dt)+Ri_w$, where L is the inductance and R the resistance of the torus. The instantaneous value of i_w can be found by integrating the above equaton and is given by

$$i_w=-\frac{V_0}{R\left[1+\left[\frac{2\pi L/R}{\tau}\right]^2\right]}\times\left[\cos(2\pi t/\tau)+\frac{2\pi L/R}{\tau}\sin(2\pi t/\tau)\ -e^{-t/(L/R)}\right], \tag{1}$$

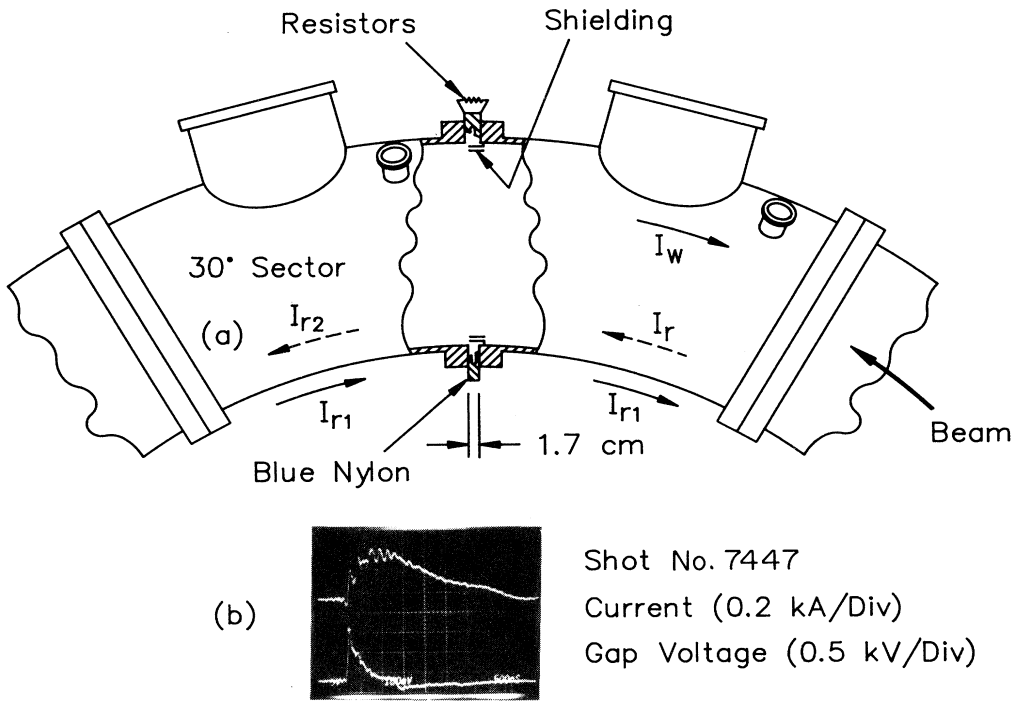

FIG. 4. (a) Schematic of the vacuum chamber joint with the insulator in place. (b) Current and gap voltage waveforms.

with the initial condition $i_w(t=0)=0$.

The temporal profile of i_w predicted by the above simple model is identical to that predicted from the exact solution of the diffusion problem for a toroidal resistive shell [16] and also is in good agreement with the results of the TRIDIF code for a finite thickness toroidal vessel. According to Eq. (1), i_w has a maximum at time t_p, which for $\alpha \equiv 2\pi(L/R)/\tau \ll 1$ is determined from $\alpha^2[1-t_p/(L/R)]=-e^{-t_p/(L/R)}$. The peak value of the current is $i_{wp}=V/R$. The measured peak value of the current in the experiment is in good agreement with the above theoretical prediction and scales, as expected, with the value of the resistance at the gap.

The return current of the beam is measured with a fast Rogowski coil ($\tau_{\text{rise}} \approx 20$ nsec) that is located outside the vacuum chamber. With the resistors at the gap shorted, the Rogowski coil shows a slowly rising current that is consistent with the decay of I_r. However, when the shorting clips are removed the Rogowski coil shows a current pulse that rises to $\sim\frac{2}{3}$ of its peak value in less than 100 nsec as shown in Fig. 4(b). The lower trace in fig. 4(b) shows the voltage across the resistors V_g as measured directly by a Tektronix 7844 oscilloscope after a $100X$ attenuation. The shape of the time-integrated V_g is very similar to the current waveform resistered by the Rogowski coil, i.e., V_g is proportional to the time derivative of the current.

COMPARISON WITH THEORY

The equations that describe the motion of the beam centroid have been solved numerically using analytical expressions for B_z and B_θ. The stellarator fields are determined numerically from Biot-Savart law by dividing each period of the windings into 20 segments. The image fields on the beam centroid have been computed analytically for a uniform density electron ring that is located inside a large major radius torus with resistive wall of thickness b-a, where a is the inner and b the outer radii of the torus. In contrast with previous calculation [12], the beam is not limited near the minor axis.

In the local cylindrical coordinate system (ρ,ϕ,z) with its origin on the geometric minor axis, the electrostatic potential inside the ring is given by [17]

$$\Phi_0=\frac{Q_l}{2\pi\epsilon_0}\left\{\ln\frac{a}{r_b}+\frac{1}{2}-\frac{1}{2}\frac{\rho^2+\Delta^2-2\Delta\rho\cos(\phi-\alpha)}{2r_b^2}+\tfrac{1}{2}\ln\left[1+\left[\frac{\Delta\rho}{a^2}\right]^2-2\frac{\Delta\rho}{a^2}\cos(\phi-\alpha)\right]\right\}, \tag{2}$$

where Δ and α define the beam position on the transverse plane, r_b is the minor radius of the beam, and Q_l is the charge per unit length. Similarly, the magnetic vector potential inside the beam is [17]

$$A_{\theta 0}=\frac{\Phi_0\beta_\theta}{c}+\sum_{k=0}^{\infty}A_{0k}U_{0k}^{(c)}(t)+\sum_{m=1}^{\infty}\sum_{k=0}^{\infty}A_{mk}\left[\frac{\rho}{a}\right]^m[U_{mk}^{(c)}(t)\cos m\phi+U_{mk}^{(s)}(t)\sin m\phi], \tag{3}$$

where β_θ is the normalized toroidal beam velocity.

The time-dependent coefficients $U_{mk}^{(c)}(t), U_{mk}^{(s)}(t)$ are zero at $t=0$ and are determined by the differential equations

$$\begin{aligned}\dot{U}_{mk}^{(c)}+\frac{1}{\tau_{mk}}U_{mk}^{(c)}&=\frac{Q_l\beta_\theta}{2\pi\epsilon_0 c\tau_{mk}}\left[\frac{\Delta}{\alpha}\right]^m\cos m\alpha,\\ \dot{U}_{mk}^{(s)}+\frac{1}{\tau_{mk}}U_{mk}^{(s)}&=\frac{Q_l\beta_\theta}{2\pi\epsilon_0 c\tau_{mk}}\left[\frac{\Delta}{\alpha}\right]^m\sin m\alpha,\end{aligned} \tag{4}$$

where

$$\frac{1}{\tau_{mk}}=\frac{\alpha_{mk}^2}{\mu_0\sigma}, \quad m=0,1,2,\ldots, \quad k=0,1,2,\ldots,$$

σ is the wall conductivity of the toroidal chamber, and α_{mk} are the zeros of the function

$$f_0(\alpha)=\frac{\pi}{2}x_0[J_1(x_0)Y_0(x_1)-Y_1(x_0)J_0(x_1)]-\frac{\pi}{2}\left[\ln\frac{8R_b}{b}-2\right]x_0x_1[J_1(x_0)Y_1(x_1)-Y_1(x_0)J_1(x_1)] \tag{5}$$

when $m=0$, and

$$f_m(\alpha)=\frac{\pi}{4}x_0x_1[J_{m+1}(x_0)Y_{m-1}(x_1)-Y_{m+1}(x_0)J_{m-1}(x_1)] \tag{6}$$

when $m=1,2,3,\ldots$. The arguments of Bessel functions in (5) and (6) are $x_0=\alpha a$, $x_1=\alpha b$ and R_b is the major radius of the beam. For each m there is an infinite number of zeros denoted by the index $k=0,1,2$. The time-dependent coefficients A_{0k}, A_{mk} that appear in the vector potential are equal to

$$A_{mk}=-\frac{2g_m(\alpha_{mk})}{\alpha_{mk}f_m'(\alpha_{mk})},$$

where $f_m'(\alpha)$ is the derivative of $f_m(\alpha)$ and

$$g_0(\alpha)=\frac{\pi}{2}[J_0(x_0)Y_0(x_1)-Y_0(x_0)J_0(x_1)]-\frac{\pi}{2}\left[\ln\frac{8R_b}{b}-2\right]x_1[J_0(x_0)Y_1(x_1)-Y_0(x_0)J_1(x_1)]$$

when $m=0$, and

$$g_m(\alpha)=\frac{\pi}{2}x_1[J_m(x_0)Y_{m-1}(x_1)-Y_m(x_0)J_{m-1}(x_1)]$$

when $m=1,2,3,\ldots$. The image fields at the beam centroid, i.e., when $\rho=\Delta$ and $\phi=\alpha$, are obtained from the expressions of Φ_0 and $A_{\theta 0}$ given above.

The radial components $B_\rho^{(c)}$ at the beam centroid is of special interest because it is responsible for the inward radial motion of the beam. This component is given by

$$B_\rho^{(c)}=\sum_{m=1}^{\infty}\sum_{k=0}^{\infty}\frac{m}{a}A_{mk}\left[\frac{\Delta(t)}{a}\right]^{m-1}\times[-U_{mk}^{(s)}(t)\cos m\alpha(t)+U_{mk}^{(c)}(t)\sin m\alpha(t)]\ . \tag{7}$$

Since $B_\rho^{(c)}$ is independent of A_{0k} and $U_{0k}^{(c)}$, i.e., it is independent of loop time $\tau_l=\tau_{00}$, the beam trapping time should also be independent of τ_l as observed in the experiment.

TABLE I. Parameters of the run shown in Fig. 5.

Torus major radius r_0	100 cm
Torus minor radius a	15.2 cm
Relativistic factor γ	1.5
SF radius ρ_0	23.4 cm
SF current I_{SF}	24 kA
Vertical field at injection B_{z0}	26 G
Toroidal field $B_{\theta 0}$	4 kG
Beam minor radius r_b	3 mm
Beam current I_b	1.2 kA
Wall resistivity	8 mΩ cm
Intermediate frequency, ω_W	1.8×10^9 sec^{-1}

To gain further insight, we have computed the image fields, including first-order toroidal corrections, at the beam centroid for a beam inside a resistive toroidal shell—in this case $B_\rho^{(c)}$:

$$B_\rho^{(c)}(\text{shell})=\frac{\sin\alpha}{R_b}\left\{\frac{Q_l\beta_\theta}{4\pi\epsilon_0 c}\left[\ln\frac{a}{r_b}+1\right]+\frac{Q_l\beta_\theta}{4\pi\epsilon_0 c}\ln\left[1-\left[\frac{\Delta(t)}{a}\right]^2\right]-\frac{Q_l\beta_\theta}{16\pi\epsilon_0 c}\left[\frac{r_b}{a}\right]^2\frac{1}{\left[1-\left[\frac{\Delta}{a}\right]^2\right]^2}\right.$$
$$\left.+\tfrac{1}{2}\sum_{m=1}^{\infty}\frac{1}{m}\left[\frac{\Delta(t)}{a}\right]^m[U_{cm}^{(0)}(t)\cos m\alpha(t)+U_{sm}^{(0)}(t)\sin m\alpha(t)]+\frac{1}{2}\left[\ln\frac{8R_b}{a}-2\right]U_0^{(0)}(t)+U_0^{(1)}(t)\right\}$$
$$+\frac{1}{a}\sum_{m=1}^{\infty}\left[\frac{\Delta(t)}{a}\right]^{m-1}\{-[U_{sm}^{(0)}(t)+U_{sm}^{(1)}(t)+V_{sm}^{(1)}(t)]\cos m\alpha+[U_{cm}^{(0)}(t)+U_{cm}^{(1)}+V_{cm}^{(1)}(t)]\sin m\alpha(t)\}\ , \tag{8}$$

where the time-dependent parameters $U_0^{(0)}(t)$, $U_0^{(1)}(t)$, $U_{cm}^{(0)}(t)$, $U_{sm}^{(0)}(t)$, $U_{cm}^{(1)}(t)$, $U_{sm}^{(1)}(t)$, $V_{cm}^{(1)}(t)$, and $V_{sm}^{(1)}(t)$ are zero at $t=0$ and are determined by the differential equations

$$\dot U_0^{(0)}+\frac{1}{\tau_l}\left[1+\tau_c\frac{\dot x_c}{R_b}\right]U_0^{(0)}=\frac{2Q_l\beta_\theta}{4\pi\epsilon_0 c}\frac{1}{\tau_l}\left[1+\frac{x_c}{2R_b}\right],$$
$$\dot U_0^{(1)}+\frac{1}{\tau_c}U_0^{(1)}=\frac{1}{2\tau_c}U_0^{(0)}\ ,$$
$$\dot U_{cm}^{(0)}+\frac{m}{\tau_c}U_{cm}^{(0)}=\frac{2Q_l\beta_\theta}{4\pi\epsilon_0 c}\frac{m}{\tau_c}\left[\frac{\Delta}{a}\right]^m\cos m\alpha\ ,$$
$$\dot U_{sm}^{(0)}+\frac{m}{\tau_c}U_{sm}^{(0)}=\frac{2Q_l\beta_\theta}{4\pi\epsilon_0 c}\frac{m}{\tau_c}\left[\frac{\Delta}{a}\right]^m\sin m\alpha\ , \tag{9}$$
$$\dot U_{cm}^{(1)}+\frac{m}{\tau_c}U_{cm}^{(1)}=-\frac{\dot x_c}{2R_b}U_{cm}^{(0)}\ ,$$
$$\dot U_{sm}^{(1)}+\frac{m}{\tau_c}U_{sm}^{(1)}=-\frac{x_c}{2R_b}U_{sm}^{(0)}\ ,$$
$$\dot V_{cm}^{(1)}+\frac{m}{\tau_c}V_{cm}^{(1)}=\frac{Q_l\beta_\theta}{16\pi\epsilon_0 c}\frac{m^2}{\tau_c}\frac{a}{R_b}\left[\frac{r_b}{a}\right]^2\times\left[\frac{\Delta}{a}\right]^{m-1}\cos(m-1)\alpha\ ,$$
$$\dot V_{sm}^{(1)}+\frac{m}{\tau_c}V_{sm}^{(1)}=\frac{Q_l\beta_\theta}{16\pi\epsilon_0 c}\frac{m^2}{\tau_c}\frac{a}{R_b}\left[\frac{r_b}{a}\right]^2\times\left[\frac{\Delta}{a}\right]^{m-1}\sin(m-1)\alpha\ ,$$

where

$$\tau_0=2\tau_c\left[\ln\frac{8R_b}{a}-2-\frac{x_c}{2R_b}\right],$$

and

$$x_c=\Delta\cos\alpha\equiv R_b-r_0\ .$$

It is apparent from Eqs. (8) and (9) that the toroidal correction term of $B_\rho^{(c)}$ is a function of τ_l. However, this term is multiplied by $\sin\alpha(t)$ and therefore averages to zero in a poloidal period.

In the limit $(b-a)\ll a$, the toroidal electric field E_θ on the outer surface of the chamber for a stationary beam has a relatively simple, closed form. At $t=0$, $E_\theta=0$ and peaks within a few fast diffusion times τ_p. For a longer time, E_θ decays to zero with τ_l. This form of the electric field is consistent with the observed return current after the beam injection. When the resistors at the gap are shorted the current measured with the external Rogowski coil should rise at the same rate the beam return current

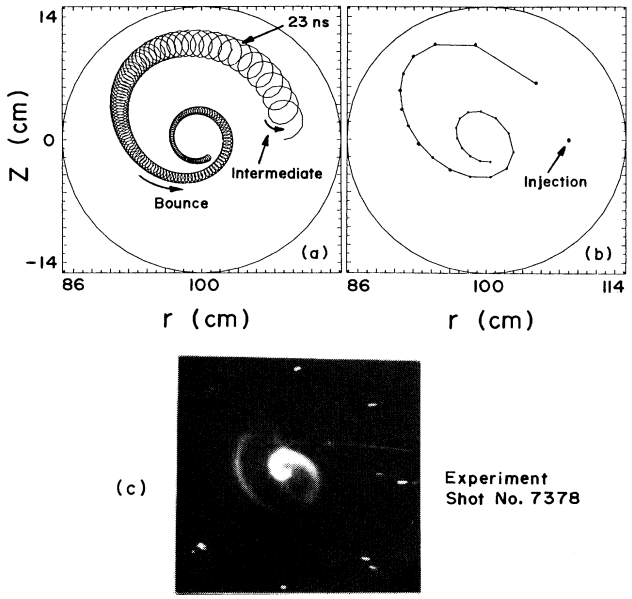

FIG. 5. Beam centroid orbit from the numerical integration of the equations of motion, using the image fields from the resistive shell model [(a) and (b)]. Results from the experiment (c).

decays. However, when the resistors at the gap are not shorted, a portion (I_{r1}) of the return current (I_r) flows on the outer wall of the chamber as shown in Fig. 4. I_{r1} rises considerably faster because the beam magnetic field can leak locally out of the resistive gap considerably faster than it can leak out of a uniform chamber.

Results from the numerical integration of orbit equations are shown in Fig. 5. The various parameters for the run are listed in Table I. Figure 5(a) shows the projection of the centroid's orbit on the $\theta=0$ plans. Both the intermediate and slow (bounce) modes are apparent. Since there are six field periods between $0\leq\theta\leq 2\pi$, the electrons perform six oscillations during one revolution around the major axis. To take into account the intermediate motion that has been neglected in the calculatoin of the image fields, the surface resistivity in the code is computed using the skin depth that corresponds to the intermediate frequency and not the actual thickness of the wall.

The solid circles in Fig. 5(b) show the positions the beam crosses the $\theta=240°$ plane. This is a realistic simulation of the experimental situation. The time difference between two circles is equal to the period around the major axis, i.e., ~23 nsec. The parameters of this run are similar to those in Fig. 5(c) and the similarity of the two orbits is quite apparent. When the crossing plane is moved from $\theta=240°$ to a different azimuthal position θ, the beam orbit rotates around the minor axis. The rotation predicted by the theory is very similar to that observed in the experiment.

There is some ambiguity, both in the experiment and theory, in the determination of the beam trapping time, because its exact value depends on the position and size of the target. However, this is not the case with τ_B, which can be measured very accurately. We made four computer runs for different values of B_θ keeping $I_{SF}/B_\theta=$constant. Figure 2(b) shows τ_B vs B_θ for three of these runs. For all practical purposes τ_B remains constant as B_θ varies. In the fourth run B_θ was reduced to 2 kG and although the beam orbit changed substantially τ_B was lower only by 7%.

As a rule, the theory predicts a τ_B and τ_{tr} that are approximately a factor of 2 shorter than those observed in the experiment. With the exception of these two times the revised model of resistive trapping is in agreement with the experiment observations, although in the analysis the beam current remains constant while in the experiment the current decays. This decay is observed whenever there is a target inside the chamber but in general is absent during the acceleration experiments when the various targets are removed.

ACKNOWLEDGMENTS

This work is supported by the Office of Naval Research and the Space and Naval Warfare Command.

*Permanent address: Science Applications International Corporation, 1710 Goodridge Drive, McLean, VA 22102.
†Permanent address: SFA, Inc., Landover, MD 20785.
‡Permanent address: FM Technologies, Inc., 10529-B Braddock Road, Fairfax, VA 22032.

[1] C. A. Kapetanakos *et al.*, Phys. Rev. Lett. **64**, 2374 (1990).
[2] H. Ishizuka *et al.*, in *Proceedings of the Seventh International Conference on High-Power Particle Beams, Karlsruhe, Germany, 1988,* edited by W. Bauer and W. Schmidt (Kernforschungszentrum Karlsruhe GmbH, Karlsruhe, 1988), Vol. II, p. 857.
[3] S. Humphries, Jr., and L. K. Len, in *Proceedings of the 1987 Particle Accelerator Conference, Washington, D.C., 1987,* edited by E. R. Lindstrom and L. S. Taylor (IEEE, New York, 1987), p. 914.
[4] V. Bailey *et al.*, in *Proceedings of the 1987 Particle Accelerator Conference* (Ref. 3), p. 920.
[5] W. K. Tucker *et al.*, in *Proceedings of the 1987 Particle Accelerator Conference* (Ref. 3), p. 957.
[6] P. Sprangle and C. A. Kapetanakos, J. Appl. Phys. **49**, 1 (1978).
[7] C. A. Kapetanakos *et al.*, Phys. Fuids **26**, 1634 (1983).
[8] N. Rostoker, Comments Plasma Phys. **6**, 91 (1980).
[9] C. Roberson *et al.*, Phys. Rev. Lett. **50**, 507 (1983).
[10] C. A. Kapetanakos *et al.*, Part. Accel. **21**, 1 (1987).
[11] C. A. Kapetanakos *et al.*, Phys. Fluids (to be published).
[12] P. Sprangle and C. A. Kapetanakos, Part. Accel. **18**, 203 (1986); Y. Seo and P. Sprangle, *ibid.* (to be published).

[13] P. Sprangle and C. A. Kapetanakos, Part. Accel. **14**, 15 (1983).
[14] L. K. Len *et al.*, in *Intense Microwave and Particle Beams,* Proceedings of the International Society for Optical Instumentation Engineers, Los Angeles, CA, January 1990 (SPIE, Bellingham, WA, 1990), Vol. 1226, p. 38.
[15] M. J. Berger and S. M. Seltzer, NASA Report No. SP-3012, 1964 (unpublished).
[16] D. Dialetis *et al.*, J. Appl. Phys. **69**, 1813 (1991).
[17] D. Dialetis *et al.* (unpublished).

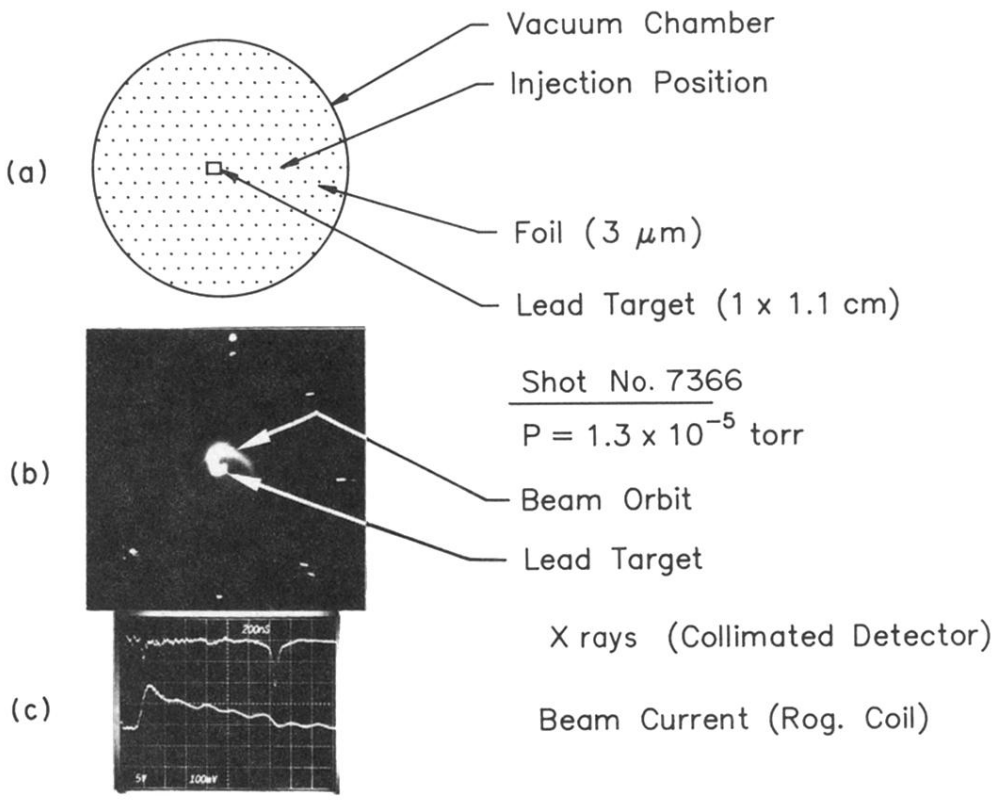

FIG. 1. Beam trapping time.

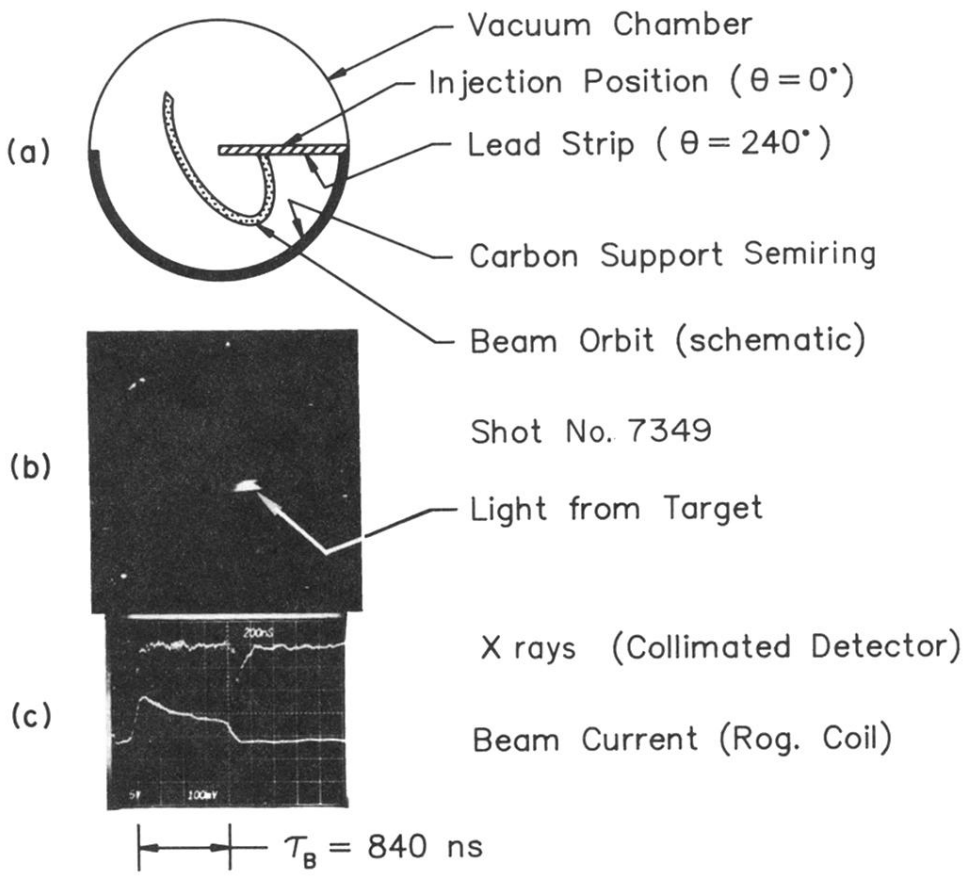

FIG. 3. Beam bounce period.

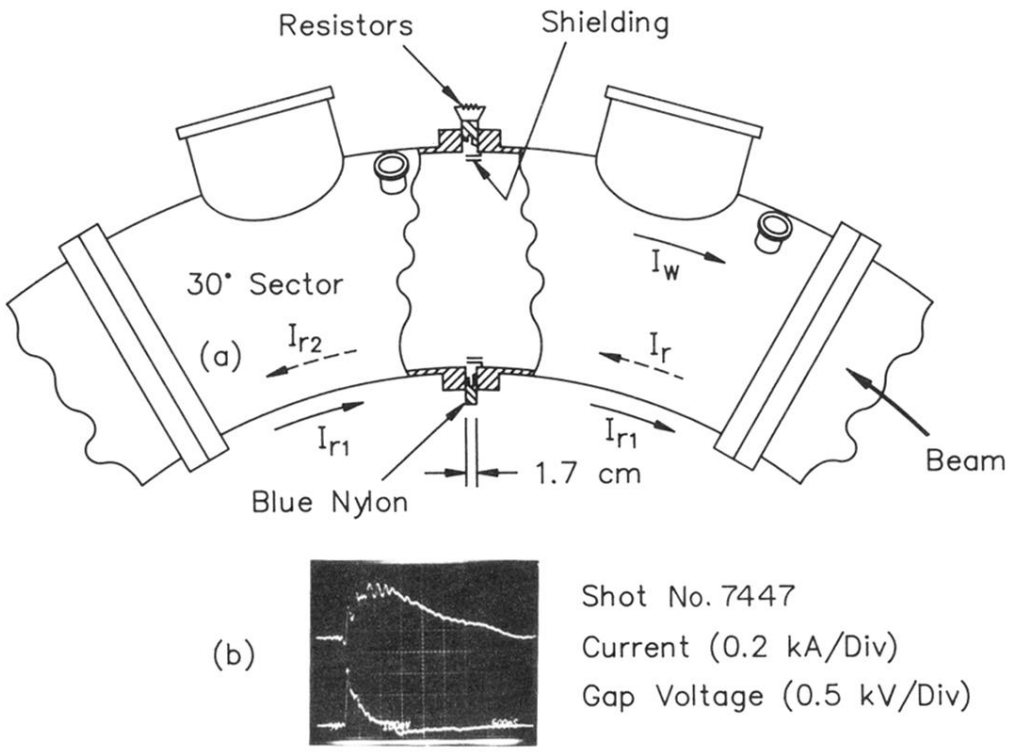

FIG. 4. (a) Schematic of the vacuum chamber joint with the insulator in place. (b) Current and gap voltage waveforms.

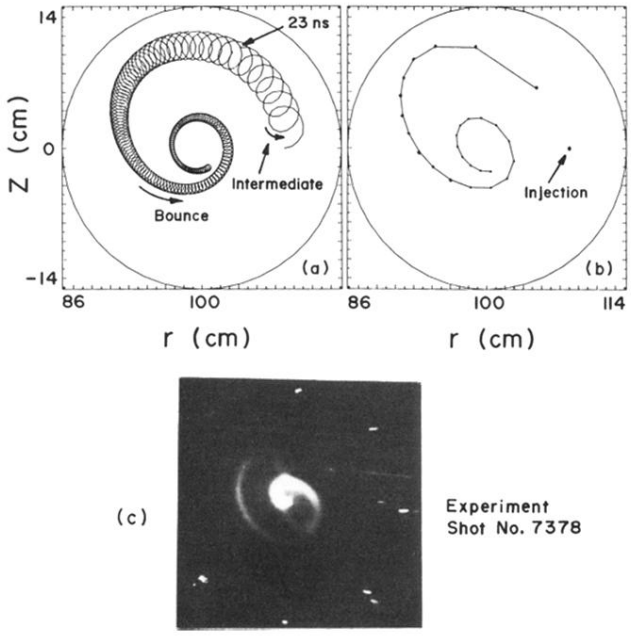

FIG. 5. Beam centroid orbit from the numerical integration of the equations of motion, using the image fields from the resistive shell model [(a) and (b)]. Results from the experiment (c).